Spider silk reinforced by graphene or carbon nanotubes - Supplementary Information

Emiliano Lepore[1], Federico Bosia[2], Francesco Bonaccorso[3,4], Matteo Bruna[3], Simone Taioli[5,6], Giovanni Garberoglio[5], Andrea. C. Ferrari[3], Nicola Maria Pugno[1,7*]

[1] Laboratory of Bio-inspired & Graphene Nanomechanics, Department of Civil, Environmental and Mechanical Engineering, University of Trento, Via Mesiano 77, 38123 Trento, Italy.
[2] Department of Physics and "Nanostructured Interfaces and Surfaces" Centre, Università di Torino, Via P. Giuria 1, 10125, Torino, Italy.
[3] Cambridge Graphene Centre, University of Cambridge, 9 JJ Thomson Avenue, Cambridge, CB3 0FA, UK
[4] Istituto Italiano di Tecnologia, Graphene Labs, Via Morego 30, 16163 Genova, Italy.
[5] European Centre for Theoretical Studies in Nuclear Physics and Related Areas, Bruno Kessler Foundation & Trento Institute for Fundamental Physics and Applications, Trento, Italy.
[6] Faculty of Mathematics and Physics, Charles University, Prague, Czech Republic.
[7] School of Engineering and Materials Science, Queen Mary University, Mile End Road, London E1 4NS, UK.
[8] Ket Lab, Edoardo Amaldi Foundation, Italian Space Agency, Via del Politecnico snc, 00133 Rome, Italy.

[*]Corresponding author: nicola.pugno@unitn.it

S1. Collection of spiders

We randomly collected 21 Pholcidae spiders (male and female of different ages). The sampling site was Torrente Chisone, between Macello and Garzigliana, Province of Torino, Italy (Geographical coordinates: 44.844 North, 7.385 East). Each spider was gently and individually segregated in a box of 19 x 12.5 x 7.5 cm^3 with four air inlets, a transparent top, white bottom and lateral sides. Spiders were transferred within 3 days from capture under an extractor fan with controlled ambient condition temperature and humidity (21.0 ± 0.2 °C and 54.3 ± 0.7 %) where they were kept during the entire experimental procedure. The procedure employed in the present study is in accordance with the Italian regulations on animal protection [1], with the relevant EU legislation and guidelines on the ethical use of animals and is approved by the local Authority Veterinary Service.

After 5 days RS samples were collected from 15 spiders. Subsequently, spiders were exposed to aqueous dispersions of graphene and CNTs, as schematically shown in Fig S1 and detailed in Table S1. We used sodium deoxycholate as surfactant for both exfoliation and dispersion of graphite and for the de-bundling of CNTs. Sodium deoxycholate is a natural bile salt [2]. Its acid, i.e., the deoxycholic acid, is one of the secondary bile acids produced in the intestine from the salts of glycocholic and taurocholic acid by means of bacterial enzymes [3]. Less than half of the sodium deoxycholate is reabsorbed by the intestine and is returned to the liver where it is conjugated and released into the gall bladder [4]. Sodium deoxycholate is often used as a biological detergent to solubilize cellular and membrane components and lyse cells [2]. Sodium deoxycholate mixed with phosphatidylcholine is used in mesotherapy injections to produce lipolysis, and has been used as an alternative to surgical excision in the treatment of lipomas [5]. Thus, we assume, due to the nature and the biological use of the surfactant, that sodium deoxycholate is not harmful for the spiders.
Nine spiders (1, 4, 5, 7, 9, 11, 13, 14, 15) started to spin silk after 2 days, while six took 12 days (2, 3, 6, 8, 10, 12). The dragline silk was then collected. Spiders 1-6 were treated with SWNT-1, 7-10 with SWNT-2, and 11-15 with graphene, as shown in Fig. S1c and Fig. S1d. After 42 days, dragline silk was collected for the second time. The silk is in the form of a single fiber composed of multiple threads. Multiple samples are obtained by cutting the fiber into 20mm-length strands for tensile tests and for the measurement of the cross-sectional area, following the procedure described in [6]. This

suggested to take adjacent samples to ensure reproducibility of fiber properties and to use one out of five samples (instead of three as here) as control to measure the fiber cross-sectional area by Field Emission Scanning Electron Microscopy (FESEM). In our work, the cross-sectional area of the fiber is determined using a FESEM without sputter coating.

ID	**Family**	**Genus**	**Species**	**sex**	**Material**
1	Pholcidae	Holocnemus	pluchei	M	SWNT-1
2	Pholcidae	Holocnemus	pluchei	M	SWNT-1
3	Pholcidae	Pholcus	opilionoides	M	SWNT-1
4	Pholcidae	Pholcus	phalangioides	M	SWNT-1
5	Theridiidae	Steatoda	sp.	M	SWNT-1
6	Theridiidae	Steatoda	triangulosa	F	SWNT-1
7	Pholcidae	Pholcus	opilionoides	M	SWNT-2
8	Pholcidae	Holocnemus	pluchei	M	SWNT-2
9	Theridiidae	Steatoda	sp.	M	SWNT-2
10	Pholcidae	Holocnemus	pluchei	M	SWNT-2
11	Pholcidae	Holocnemus	pluchei	M	GRAPHENE
12	Pholcidae	Holocnemus	pluchei	M	GRAPHENE
13	Pholcidae	Holocnemus	pluchei	M	GRAPHENE
14	Pholcidae	Holocnemus	pluchei	M	GRAPHENE
15	Pholcidae	Holocnemus	pluchei	M	GRAPHENE

Table S1: *Spider types used in experiments and nanomaterial solution they were exposed to.*

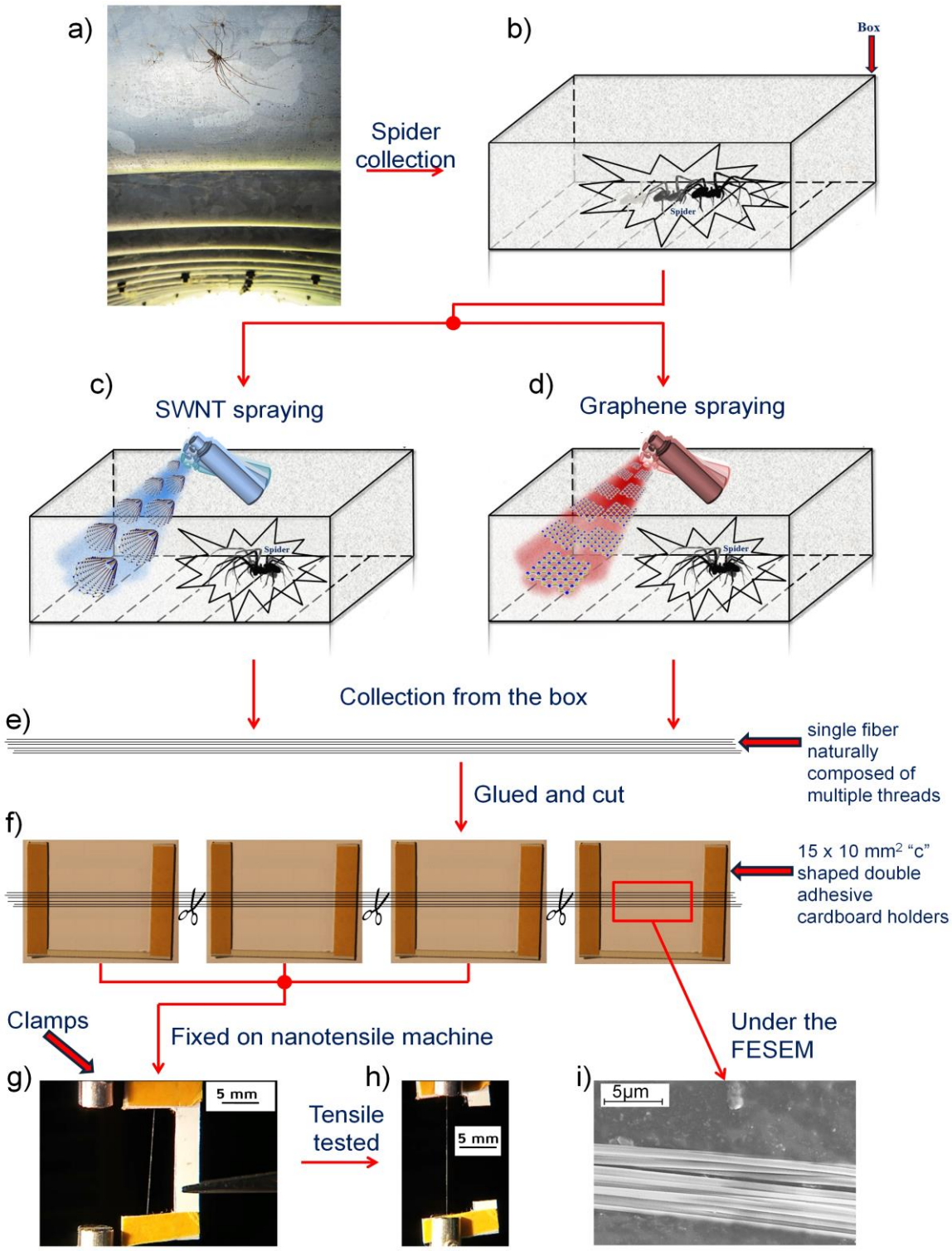

Figure S1: ***Schematic illustration of the experimental procedure.*** *(**a**) Sampling site and experimental box for the collection of (**b**) RS samples and, after spraying with (**c**) CNTs or (**d**) graphene dispersions. (**e**) Collection of silk in the form of a single fibre, composed of multiple threads, from which multiple samples are obtained by fixing the ends of the fibre to 15 x 10 mm² "c" shaped double adhesive cardboard holders and (**f**) cutting the fibre into four shorter pieces, (**g**) mounted on nanotensile machine clamps (**h**) for nanotensile tests and (**i**) for measuring the fibre cross-sectional surface area with a FESEM. Scale bar 5 µm.*

S3. Characterization

S3.1 Optical absorption Spectroscopy

S3.1.1 Optical absorption spectroscopy of SWNTs

Optical absorption spectroscopy (OAS) reveals various properties of SWNT dispersions such as transition energies [7, 8] bundling [9] and concentration [10].

Spectra are acquired in a Perkin Elmer 950 with 1nm resolution. Measurements are carried out in the range 400-1300nm, limited by the strong absorption features of water [11]. However, this range is sufficient to cover the first and second excitonic transitions of s-SWNTs [12, 13] and the first transition of m-SWNTs, for CoMoCAT [12, 13] and the second and third transitions of s-SWNTs and first of m-SWNTs [14, 15] for the P2 samples. Absorption from solvent and surfactants is subtracted, by measuring solutions with only solvent and surfactant.

The assignment of the optical transitions is based on the empirical Kataura plot of Ref. [15]. This gives values of optical transition frequencies versus chirality for SWNTs in aqueous surfactant dispersions, and is more appropriate than Kataura plots theoretically derived from tight binding and other models [16].

The OAS of SWNT-1 and SWNT-2 are reported in Fig. S2. SWNT-1 have sharper peaks with respect to SWNT-2 sample. The OAS of SWNT-1 shows the M_{11} region as well as the eh_{11} and eh_{11} regions, while SWNT-2 shows the M_{11} region as well as the eh_{22} and eh_{33} regions.

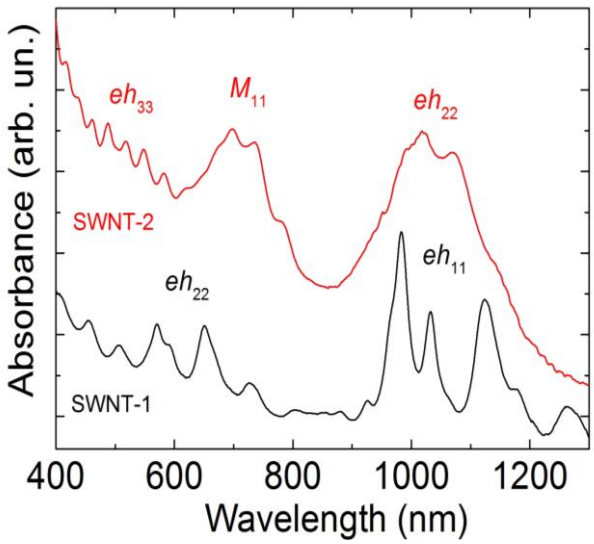

Figure S2: *Absorption spectra of SWNT-1 (black curve) and SWNT-2 (red curve). The labels eh_{11}, eh_{22}, eh_{33} and M_{11} refer to the first, second, third semiconducting and the first metallic excitonic transition, and are a guide to the eye, since overlap between different excitonic transitions exists [14, 15]. The spectra are normalized for a clear visualization.*

S3.1.1 Optical absorption spectroscopy of graphitic flakes

Fig. S3 report the absorption spectrum of the graphene dispersion. The peak at ~266 nm is a signature of the van Hove singularity in the graphene density of states [17]. OAS used to evaluate the concentration of graphitic material in dispersion, using the experimentally derived absorption coefficient of $1390 Lg^{-1}m^{-1}$ at 660nm [18, 19], we estimate concentration ~0.03mg/ml.

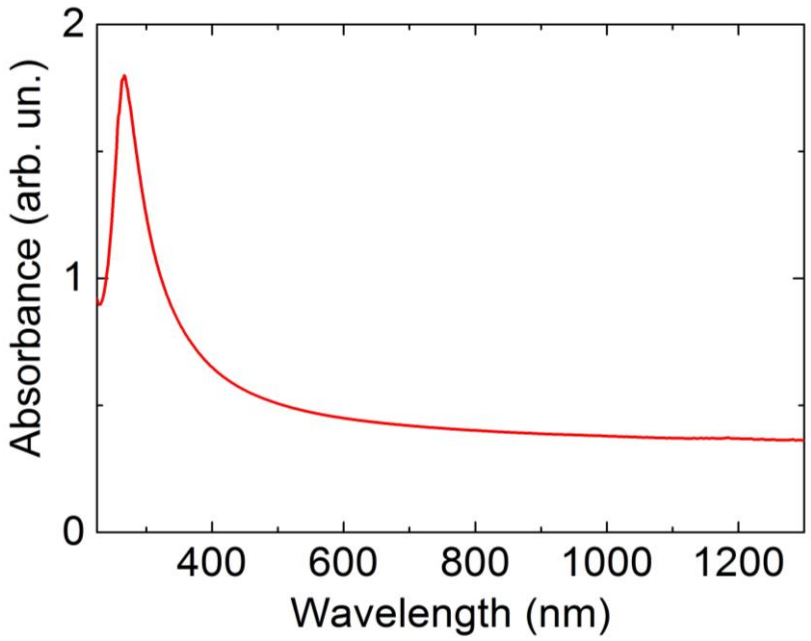

Figure S3: *Optical absorption spectrum of graphene dispersion in water with SDC surfactant.*

S3.2 Raman Spectroscopy

S3.2.1 Pristine SWNTs

Raman spectroscopy can be used to probe SWNTs within dispersions. In the low frequency region, the Radial Breathing Modes (RBMs) are observed [20]. Their position, Pos(*RBM*), is inversely related to SWNT diameter, *d* [21-23], as given by:

$$Pos(RBM) = \frac{C_1}{d} + C_2$$

.

Combining Pos(*RBM*), with excitation wavelength and the '*Kataura plot*' [15], it is, in principle, possible to derive the SWNT chirality [24, 25].

Matching the diameter with excitation wavelength in the Kataura plot also gives information on the semiconducting or metallic character. A variety of C_1 and C_2 were proposed for this relation [7, 8, 14, 26]. Here we use the $C_1 = 214.4\ cm^{-1}$ nm and $C_2 = 18.7\ cm^{-1}$, from Ref [27]. These were derived by plotting the resonance energy as a function of inverse RBM frequency without additional assumptions. We also validated our results by using the parameters proposed in Refs. [7, 10], [28].

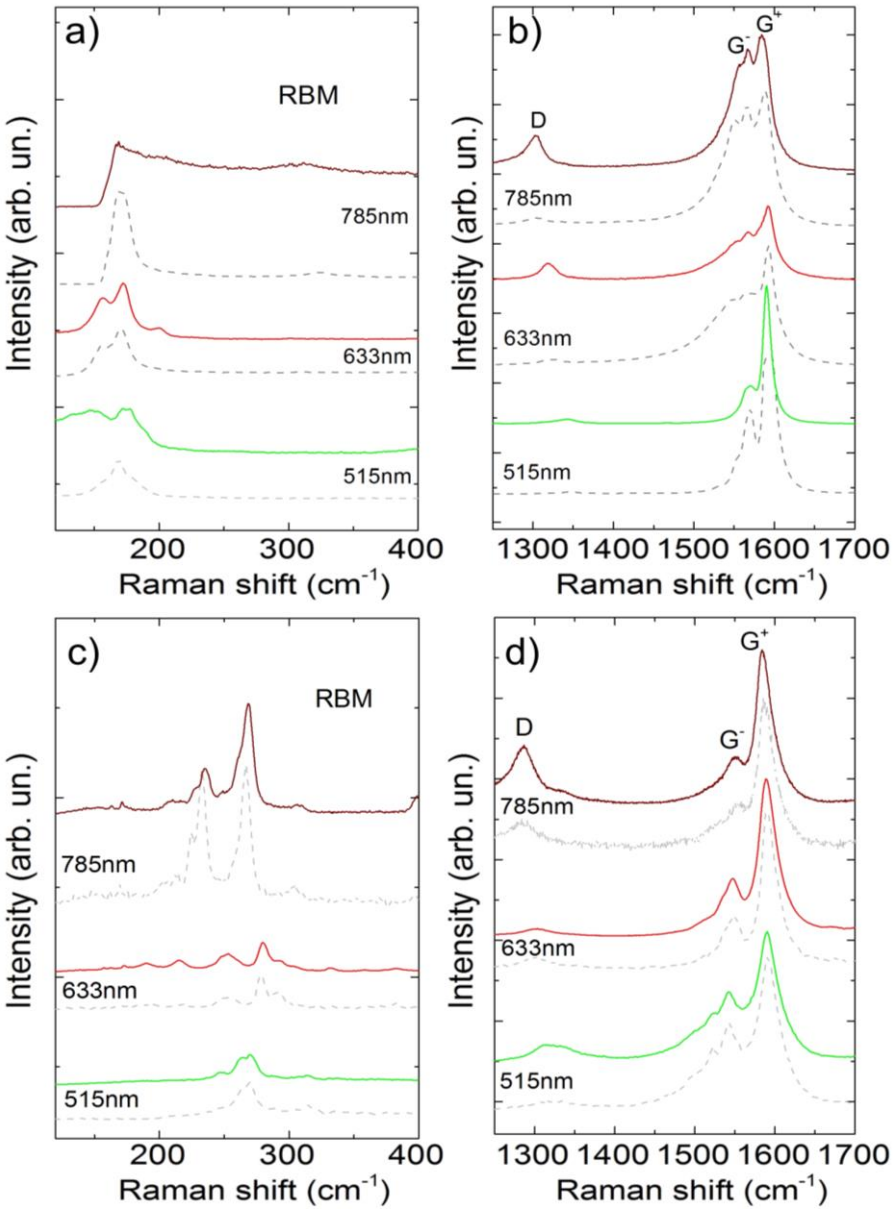

Figure S4: *Raman spectra of SWNTs at different excitation wavelengths: 514.5nm (green curve), 633nm (red curve) and 785nm (brown curve) (a) RBM and (b) G region for SWNT-1 and (c) RBM and (d) G region for SWNT-2. The Raman spectra of the starting materials (powders) are reported in light grey dashed lines below each curve for comparison.*

Raman spectroscopy also probes possible damage via the *D* peak [29]. The *D* peak is due to the breathing modes of sp^2 rings and requires a defect for its activation by double resonance (DR) [30, 31]. The typical Raman spectrum of SWNTs in the 1500-1600 cm^{-1} region consists of the G^+ and G^- bands. In s-SWNTs, they originate from the longitudinal (LO) and tangential (TO) modes, respectively, derived from the splitting of the E_{2g} phonon of graphene at the Brillouin zone centre [32-34]. The positions of the G^+ and G^- peaks, Pos(G^+), Pos(G^-), are diameter dependent and their separation increases with decreasing diameter [35, 36]. In m-SWNTs, the assignment of the G^+ and G^- bands is the opposite, and the FWHM of the G^- peak, FWHM(G^-), is larger and Pos(G^-) down-shifted with respect to the semiconducting counterpart [20, 37]. Thus, a wide, low frequency G^- is a fingerprint of m-SWNTs. On the other hand, the absence of such a feature does not necessarily imply that only s-SWNTs are present, but could signify that m-SWNTs are off-resonance.

Doping could also modify positions and FWHMs [38, 39]. In m-SWNTs, a Pos(G^-) blueshift, accompanied by a FWHM(G^-) decrease is observed with electron or hole doping[40, 41]. In s-SWNTs, doping upshifts Pos(G^+), but does not affect FWHM(G^+) [14, 23].

Thus, a large number of excitation wavelengths are necessary for a complete characterization of SWNTs [18, 42]. Nevertheless, useful information can be derived even with few excitation wavelengths.

Raman spectra are taken on both the starting materials (powder) and the dispersions, deposited by drop-casting onto an aluminium substrate to avoid any Raman background, with a Renishaw system at 514.5 nm (2.41 eV) 633 nm (1.96 eV) and 785 nm (1.58 eV), using a 100X objective and a less than 1 mW on the sample. The RBM detection is limited by the cut-off of the notch and edge filters. These are at 120, 100 and 110 cm^{-1} for 514, 633 and 785nm, respectively, limiting the detection to diameters up to ~1.9nm.

The RBM spectra of the SWNT-1 in Fig. S4(a) show a distribution, spanning the 175–370 cm^{-1} range both for the starting material and the dispersion, considering the peaks for the three excitation wavelengths. This RBM range corresponds to SWNTs with ~0.6–1.35nm diameter. Fig. S4(b) plots the spectra in the G region of SWNT-1. A weak D band is observed [I(*D*)/I(*G*)~0.13], indicating small number of defects [15, 16]. These defects could be induced by the ultrasonication process because the I(*D*)/I(*G*)~0.05 of the powder is lower with respect to the dispersion.

The RBM spectra of the SWNT-2 in Fig. S4(c) show a similar distribution but peaked at lower wavenumbers with respect to SWNT-1. Indeed, the RBMs span the 150–215 cm^{-1} range both for the starting material and the dispersion, considering the peaks for the three excitation wavelengths. This corresponds to SWNTs with ~1.05–1.65nm diameter. Fig. S4(d) plots the spectra in the G region of SWNT-1. A weak D band is also observed [I(*D*)/I(*G*)~0.18] for the SWNT-2 sample, indicating small number of defects [15, 16]. As for the SWNT-1, also in the case of the SWNT-2 sample, these defects could be induced by the ultrasonication process because the I(*D*)/I(*G*) ~0.08 of the powder is lower with respect to the one of the dispersion.

S3.3 Pristine flakes and dispersions

The ultracentrifuged dispersions are drop-cast onto a Si wafer with 300nm thermally grown SiO_2 (LDB Technologies Ltd.). These samples are then used for Raman measurements at 488, 514.5, and 633nm. The G peak dispersion is defined as $Disp(G) = \Delta Pos(G)/\Delta\lambda_L$, where λ_L is the laser excitation wavelength.

Fig. S5a plots a typical Raman spectrum of the flakes prepared on Si/SiO_2 substrates.

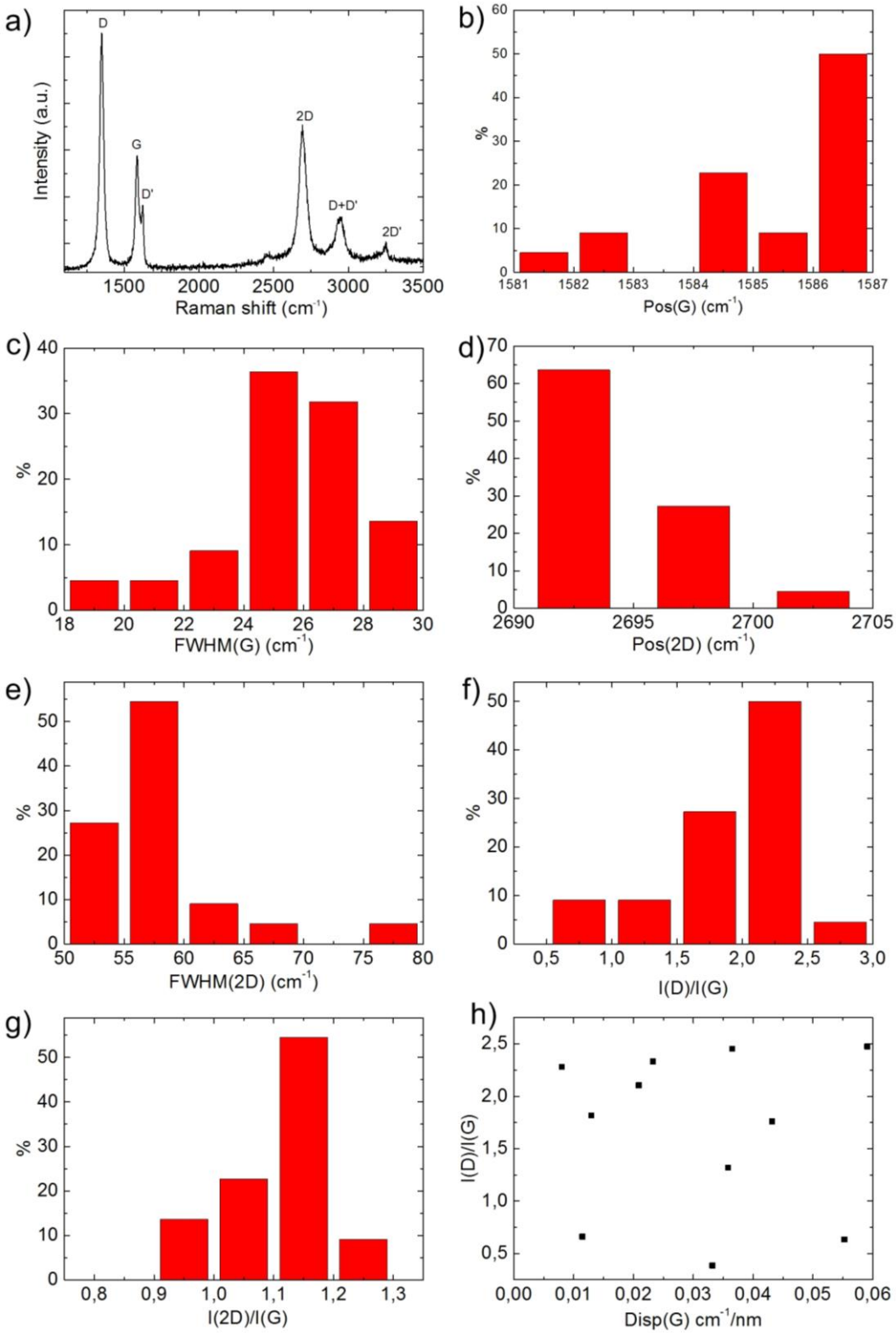

Figure S5: *a) Raman spectrum measured at 514.5nm excitation for a representative flake obtained via LPE of graphite. Distribution of b) Pos(2D), c) FWHM(2D), d) Pos(G), e) FWHM(G), f) I(D)/I(G), g) I(2D)/I(G), and h) distribution of I(D)/I(G) as a function of Disp(G).*

Besides the *G* and 2*D* peaks, this spectrum shows significant *D* and *D'* intensities and the combination mode *D*+*D*'. Statistical analysis of the spectra shows that Pos(*G*) (Fig. S5b) and FWHM(*G*) (Fig. S5c) are ~1582 and ~27cm^{-1}. Pos(2*D*) peaks ~2695cm^{-1} (Fig. S5d), while FWHM(2*D*) varies from

50 to 80cm^{-1} (Fig. S5e) with a peak at 57cm^{-1}. This is consistent with the samples being a combination of single- (SLG) and few-layer (FLG) graphene flakes. The Raman spectra show significant *D* and *D*' intensities, with the intensity ratio I(*D*)/I(*G*) having a maximum at 2.25 (Fig. S5f). This high I(*D*)/I(*G*) is attributed to the edges of our sub-micrometer flakes [43], rather than to the presence of a large amount of structural defects within the flakes. This observation is supported by the low Disp(*G*)<0.06 cm^{-1}/nm, much lower than what expected for disordered carbon [31]. Combining I(*D*)/I(*G*) with Disp(*G*) allows us to discriminate between disorder localized at the edges and disorder in the bulk. In the latter case, a higher I(*D*)/I(*G*) would correspond to higher Disp(*G*). Fig. S5h show that Disp(*G*) and I(*D*)/I(*G*) are not correlated, an indication that the major contribution to the *D* peak comes from the edges of the sample.

S.4 High Resolution Transmission Electron Microscopy

We analysed the samples with High Resolution Transmission Electron Microscopy (HR-TEM) to determine the spatial distribution of the carbon nanoreinforcements. As shown in Fig. S6, carbonaceous material was observed between different fibers. Some crystalline graphitic material was observed in this area. However, from Fig. S6 it is not possible to observe the spatial ordering of individual CNTs or graphene inside the silk matrix. We note that Ref. [44] shows a very similar TEM image that also fails to provide evidence of the structure at nanoscale. The authors claim that "silk fibers show regions with highly ordered graphitic structures", but this ordering is not at all apparent in these images, nor is the deep integration of the nano-reinforcements in the silk amourphous matrix.

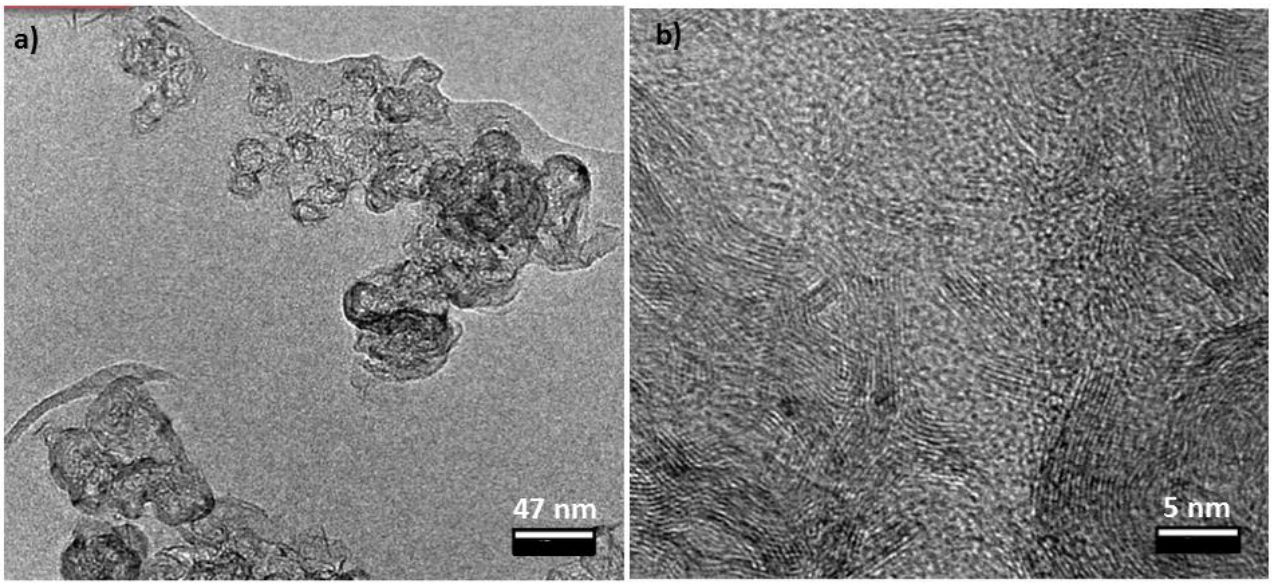

Figure S6: *HR-TEM images of the Graphene-reinforced silk at two different magnification levels.*

S.4 Nanotensile Tests

Nanotensile tests are performed under controlled laboratory conditions, since any change in temperature and humidity may affect the mechanical characteristics of the silk threads [45-48].

We monitor the experimental ambient conditions with a datalogger (EL-USB-2, Lascar Electronics): the air temperature and the relative humidity were recorded to be 22.8 ± 1.3 °C and 59.1 ± 5.0 %. We fixed silk fibre ends to 15 x 10 mm^2 "c" shaped cardboard holders, with double adhesive faces. These allowed the fibre to be suspended and mounted on the nanotensile testing machine, while maintaining its original tension without damage (Fig. S1g). The tests are conducted using a nanotensile testing system (T150, Agilent, Santa Clara, USA), equipped with 500 mN maximum cell load. This can generate load-extension data with a load resolution of 50 nN and a 0.1nm displacement

resolution. Cardboard holders are placed between the clamps. Once the holders are in place, the clamps are closed and one side of the holders is cut (Fig. S1h), leaving the fibre free between the clamps. We perform a continuous dynamic analysis of the silk by imposing an oscillating dynamic strain up to failure of the thread. We use a dynamic strain oscillation with a 20Hz frequency and a 0.1mN dynamic force amplitude, which enable mechanical properties to be determined continuously.

Typical stress-strain results for tests on various silk samples from the first 14 spiders are shown in Fig. S6 before and after exposure to the nanomaterial dispersions. The results are discussed in the Main Text.

We do not consider the effect of the nano-reinforcement volume fraction on the variation of density, since this is negligible for the considered volume fractions. In CNTs, the density ρ_{CNT} is between 1.3 and 1.4 g/cm^3 [49], similar to that of silk (1.34 g/cm^3 [50]). In the case of graphene, the density is close to that of graphite, i.e. ρ_G ~2.1 g/cm^3 [51-53], so the effect would be a slight increase in the overall density, and thus a small reduction in toughness modulus. For a very high f = 12% volume fraction of nano-reinforcements (usually the onset of agglomeration effects determining a deterioration of reinforcement properties occurs below 10%), there is an increase in density from ρ_S = 1.34 g/cm^3 for the pristine silk to ρ_{TOT} = 1.34 g/cm^3 and ρ_{TOT} = 1.43 g/cm^3 when CNTs or graphene are added (estimated using a simple rule of mixtures: $\rho_{TOT} = (1-f)\rho_S + f\rho_{CNT/G}$) corresponding to a 0.1% and 6.7% decrease of toughness modulus, respectively. Should CNTs and graphene additionally cause an increase in volume, this would contribute to a reduction in the overall density, therefore an increase of the toughness modulus. In any case, it is likely that these limited silk density variations would be smaller than the variations due to humidity mentioned in the main text [54], and can thus be neglected in the estimation of toughness moduli.

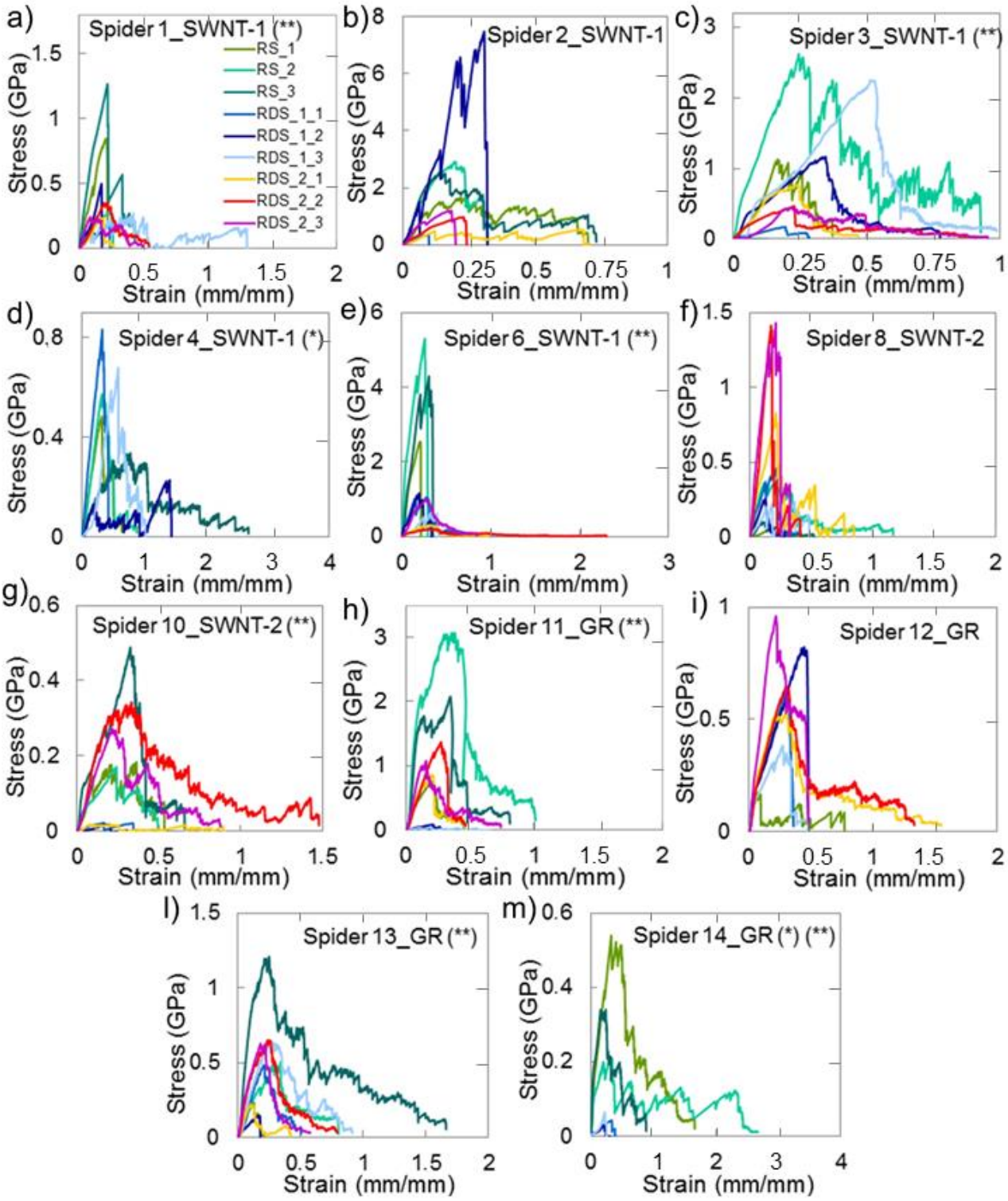

Figure S7: ***Stress-strain curves.*** *Stress-strain curves for silk produced by spiders after first (RDS_1) or second (RDS_2) ingestion of a-g) SWNT-1, SWNT-2 or h-m) graphene dispersions. The symbol "**" specifies enhanced mechanical properties (fracture strength and Young's modulus) after first collection. The symbol "*" specifies that spiders died before the second collection.*

A further collection of silk was carried out after a few days, but the corresponding samples did not display mechanical improvements with respect to the first or to RS, probably due to a physiological spider weakening during segregation, since neither additional food nor water were available during the experimental period, except SWNTs and graphene dispersions. Results are

reported in Table S2. In the cases marked with an asterisk in Figs. S6, the second collection was impossible since the corresponding spiders died. Note that spider 5 died after the first treated dragline silk collection, but was able to spin the silk with the maximum increment in mechanical performance, whereas spider 7 spun the silk with the highest absolute values and survived.

Spider n.	Diameter (μm)	Number of threads	Reinforcement	Young's Modulus (GPa)	Ultimate Strain (mm/mm)	Fracture Strength (MPa)	Toughness Modulus (MPa)
1	0.658±0.063	73	SWNT-1	2.8±1.1	0.423±0.142	275.1±65.5	55.3±26.9
2	0.410±0.023	27	SWNT-1	9.5±6.4	0.368±0.274	906.2±338.5	168.1±36.5
3	0.587±0.041	96	SWNT-1	5.1±0.7	0.753±0.258	562.5±178.5	157.4±10.4
4	-	-	SWNT-1	-	-	-	-
5	-	-	SWNT-1	-	-	-	-
6	1.071±0.140	160	SWNT-1	3.6±2.4	1.325±0.781	507.6±429.8	198.1±115.1
7	1.013±0.150	330	SWNT-2	3.6±1.8	0.818±0.386	473.1±273.0	195.6±163.6
8	0.180±0.020	58	SWNT-2	9.9±3.1	0.509±0.272	1222.8±341.9	196.9±41.1
9	-	-	SWNT-2	-	-	-	-
10	0.550±0.162	114	SWNT-2	1.4±0.9	1.055±0.325	211.2±171.0	99.6±95.8
11	0.413±0.056	89	GS	8.6±2.2	0.540±0.153	1102.5±255.7	241.4±69.4
12	0.640±0.056	240	GS	5.6±2.1	1.082±0.554	716.7±216.2	286.7±24.4
13	0.586±0.074	144	GS	5.6±1.4	0.577±0.171	499.6±240.3	125.7±85.8
14	-	-	GS	-	-	-	-
15	0.533±0.118	153	GS	2.5±1.8	1.138±0.465	216.9±132.0	110.4±101.4

Table S2. *Mechanical properties (average values) of the second collection of silk samples produced after exposure of the spiders to the SWNT and graphene dispersions. 26% of the spiders died between the first and second collections, thus the corresponding data are absent.*

Table S3 shows average values for similar types of silk found in the literature [55-57], and their corresponding standard deviations, showing that uncertainties are in many cases comparable to those in this work.

Source	Young's Modulus (GPa)	Ultimate Strain (mm/mm)	Fracture Strength (MPa)	Toughness Modulus (MPa)
This work	10.73±4.84	0.70±0.35	1082.94±504.48	313.70±204.78
Ref [55]	11.11±3.67	0.22±0.05	1095.17±296.12	125.49±42.87
Ref [56]	10.08±1.32	0.30±0.02	986.5±107.25	194.8±23.2
Ref [57]	11.50±3.85	0.62±0.15	1634.00±323.67	217.00±84.33

Table S3. *Average mechanical properties for spider silks in the literature, compared to those found in this work*

S.6 Statistical data analysis and numerical HFBM simulations

Analysis of experimental data discussed in the Main Text and in the "Nanotensile Tests" Section indicates that there is a large statistical spread in the measured mechanical properties of RS as well as CNTS and GS. In the case of GS and CNTS it is not possible to compare samples from different spiders, since their concentrations are different, so that samples belong to different statistical populations. On the RS samples, a statistical analysis of the experimental data is performed to verify if they belong to the same statistical population, despite deriving from different spider species. To do this, we adopt the Weibull distribution, which is widely used in fracture mechanics and particularly suitable to describe dispersion of mechanical properties [58], and fit the data relative to RS. The resulting 2-parameter Weibull distributions are shown in Fig. S8. The parameters for the corresponding Weibull distributions of RS are summarized in Table S4. Scale parameters are indicative of average values, whilst shape parameters are correlated to the dispersion of the distributions.

RS	Mean	STD	Shape parameter	Scale parameter
Young's Modulus (GPa)	10.73	10.43	1.19	11.06
Strength (MPa)	1082.94	1082.94	1.27	1126.55
Ultimate Strain	0.70	0.40	2.09	0.79

Table S4. *Mean Young's modulus, strength and ultimate strain of RS and corresponding Weibull parameters.*

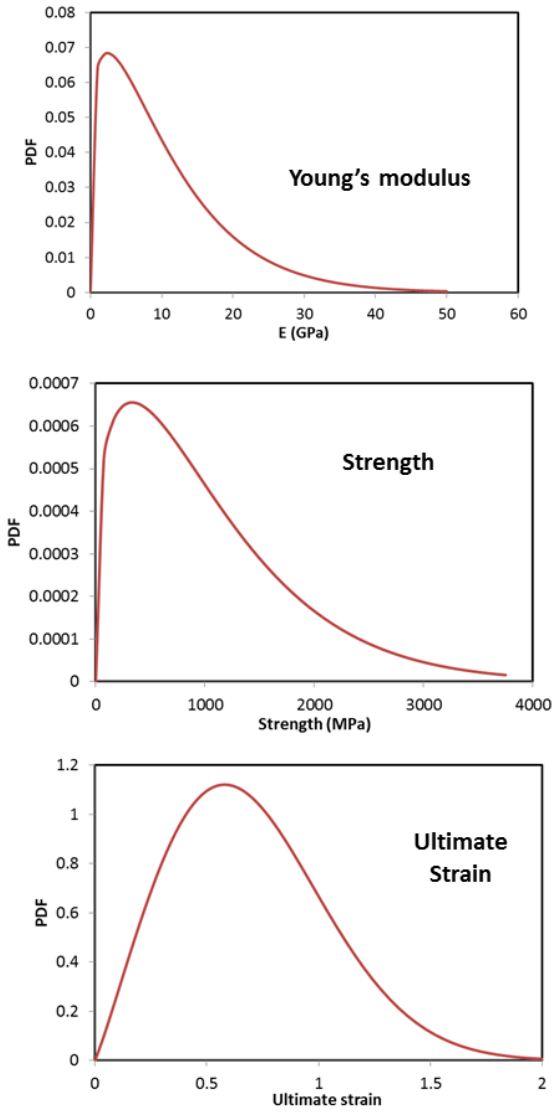

Figure S8: Weibull fits for mechanical data on RS. *Weibull fits (Probability Density Functions, PDF) on experimental data for a) Young's modulus, b) strength and c) ultimate strain of RS.*

Numerical simulations of deformation and fracture are performed using the Hierarchical Fibre Bundle Model (HFBM) [59], whereby the macroscopic fibres are modelled as networks of microfibres and/or reinforcements arranged in parallel and in series, subjected to uniaxial tension. The microfibers are treated as elastic springs with statistically distributed fracture strengths, according to measured or known input parameters for the constituents (i.e. the experimentally-determined Weibull parameters from Table S.4 for the silk, and known mechanical properties from the literature for CNTs and graphene). As in all fibre bundle models, interfacial interaction between threads in a bundle is neglected, apart from load redistribution after failure of a single thread. This is akin to neglecting shear effects. However, this was shown to be a reasonable approximation in the case of tensile testing of this type of fibre as discussed in Ref. [59]. The statistical distribution of strengths in the fibres forming a bundle reproduces correctly the fracture behaviour of individual macroscopic fibres due to microcracking. Simulations are carried out in a multiscale procedure, from single SWNT (diameter ~1.5 nm, length ~250 nm) scale to the macroscopic scale of specimens used in experimental tests (diameter ~ 5 μm, length ~1 cm). The silk/silk and silk/nanoparticle interaction (in terms of load redistribution) is modelled only at the lowest hierarchical level. At higher hierarchical levels the fibre

is considered as consisting of homogeneous threads. The typical number of fibres used in upper hierarchical level simulations is 10^3 (this is to be interpreted as a discretization parameter used to simulate damage progression). We consider typical values for SWNT and graphene properties, respectively: Young's modulus $E_{CNT} = E_{SLG} = 1$ TPa [60, 61] and strength $\sigma_{CNT} = 45$ GPa [60], $\sigma_{SLG} = 130$ GPa [61]. The experimentally obtained RS Weibull distributions are used as input properties. Figure 9 shows typical simulations results for stress-strain curves with different SWNT volume fractions V_f, assuming a uniform SWNT dispersion at the lowest hierarchical simulation level (i.e. that at which individual SWNTs coincide with springs in the bundle). Figure S10 indicates that there is an overall strength and modulus increase with increasing V_f, while there is a corresponding ultimate strain reduction. As a reference, comparisons are made with rules of mixtures (RM, see Fig. S10). As expected, HFBM predictions for strength lie between direct and inverse rule of mixtures predictions.

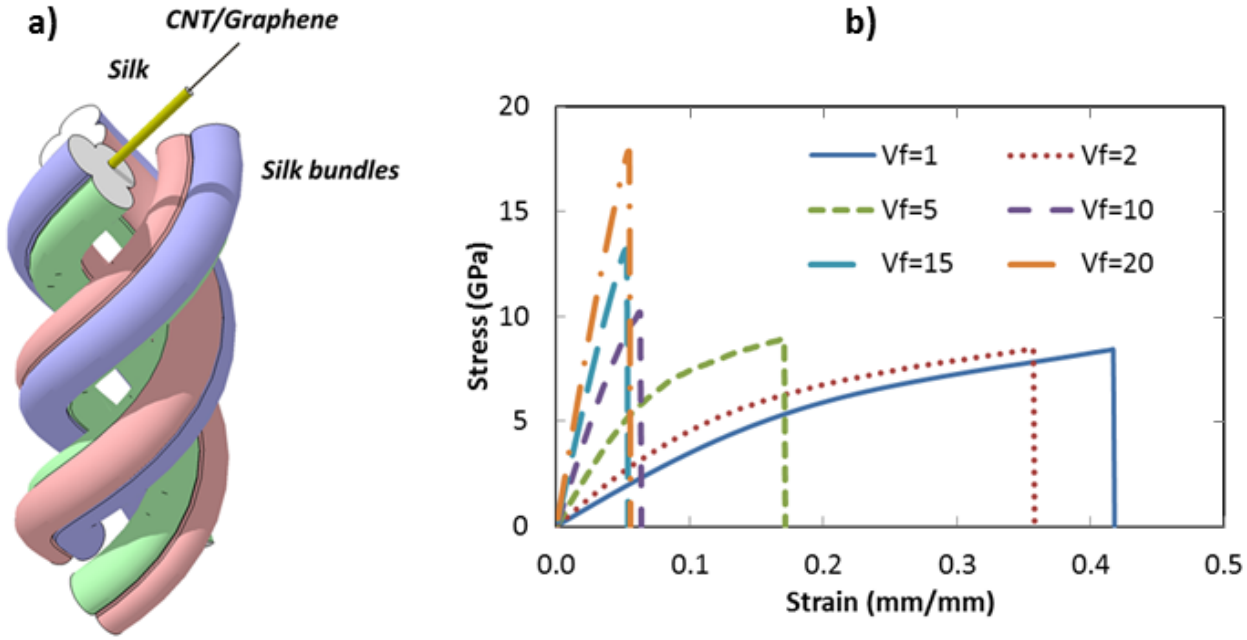

Figure S9: HFBM simulations. *a) Schematic of the model and b) examples of stress-strain results for different volume ratios.*

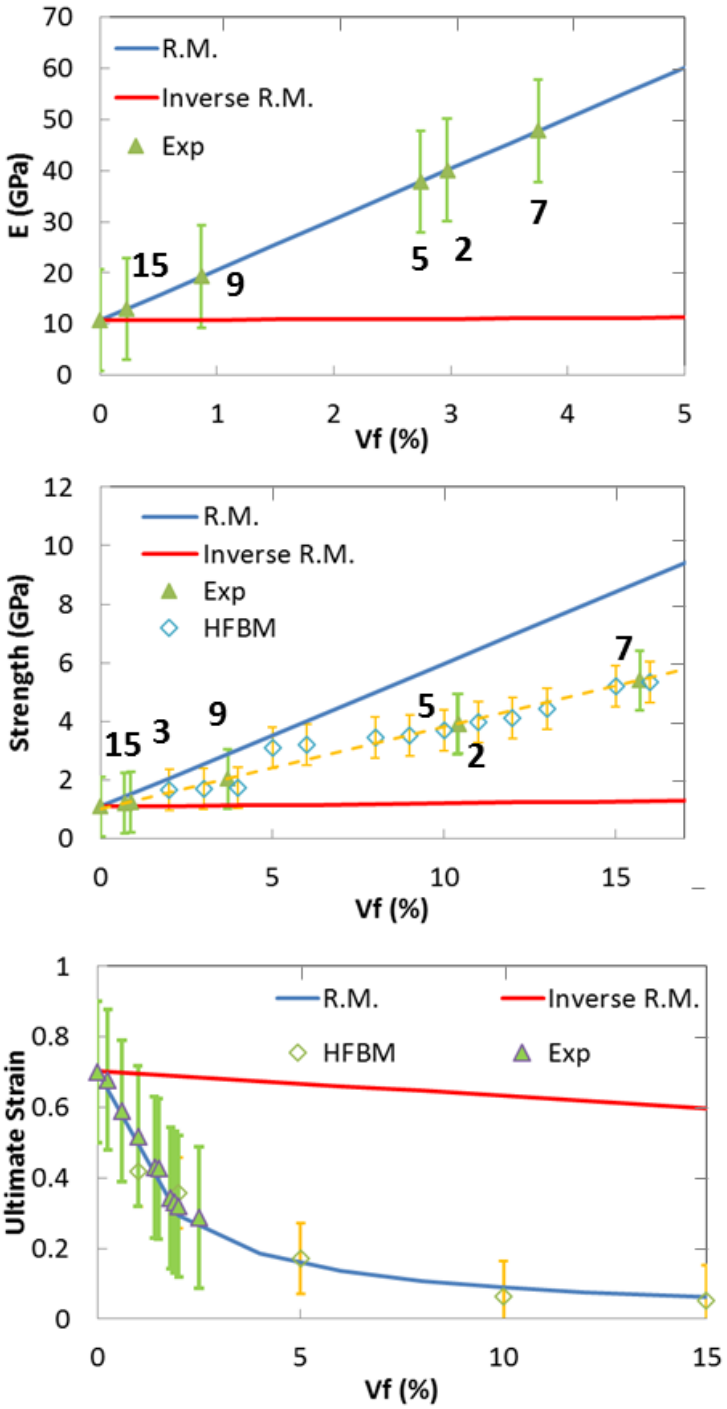

Figure S10: Comparison of experiments with HFBM simulations and direct or indirect rules of mixture (RM). *RM predictions are shown as blue lines (direct RM law, taken as an upper bound for predictions) and as red lines (inverse RM law, taken as lower bound for the predictions). Experimental data are plotted as green triangles, with corresponding sample numbers, and with error bars corresponding to the experimental standard deviations (with V_f values estimated from RM or HFBM, as explained below), while HFBM data are shown as hollow diamonds, with error bars corresponding to uncertainties due to statistical variations in the simulations. Only experimental data compatible with a rule of mixtures V_f estimation. i.e., with improved properties with respect to RS, are shown. These values are "effective" in the sense that they consider also the expected sik modification around the nanoparticles. For ab initio simulations see [62].*

S.7 Atomistic simulations of the mechanical properties of spider silk

We perform classical molecular dynamics simulations in order to obtain a qualitative understanding of the CNT and graphene's interaction with the silk proteins. We generate a model of the MASP1 spider silk protein as in Refs. [63, 64]. We use the CHARMM27 force field implemented in GROMACS (v. 4.6.7) [65] to model the molecular interactions. In order to have a charge-neutral system we substitute arginine with glutamine (the neutral aminoacid with the closest structure). The final aminoacid sequence of the fiber is:

GGAGQGGYGGLGSQGAGQGGLGGQGAGAAAAAAGGAGQGGYGGLGSQGAGQGGLGGGAG.

From this, we generate a fully extended MASP1 fiber using OpenBabel (v. 2.3.2) [66], from which a bundle of 15 fibers (aligned along the x direction) is prepared by translation and inversion to facilitate the formation of the central ordered region. Initially, the fibers are kept separate (1 to 2 nm), so as to be able to insert graphene or CNTs in the amorphous region and to prevent the disruption of the crystalline poly-alanine core. In simulations, we used capped nanotubes with a diameter of ~0.8 nm, which is comparable to the experimental value of ~0.6–1.35 nm for SWNT-1 and ~1.05–1.65 nm for SWNT-2. The length of 1.8 nm of the CNTs in simulations was chosen so to have dimensions smaller/comparable to the disordered part of the modelled fiber (around 3.5 nm over a total fiber length of about 11 nm, see Fig. S11 a). This is much smaller than the experimental value. Within the accuracy of the chosen silk model [63, 64], the interaction between CNTs and fiber scales linearly with the CNT length since the adopted interatomic potential is pair-wise and the CNTs can be considered essentially one-dimensional. Based on this argument, the interaction per unit cell can be considered nearly invariant with the CNT length, and in our investigation, we take a CNT length that reproduces a characteristic CNT volume fraction of f = 12% (see macroscopic simulations in section S6, where the CNT length is taken to be 250 nm). The same arguments apply for the graphene flakes, which are thus modeled as square-shaped sheets with a lateral dimensions of ~2 nm (much smaller than the experimental dimensions). CNTs and graphene are modeled using the DREIDING force field to account for their flexibility and the interaction with the protein's atoms. This initial configuration is equilibrated using the following procedure: after a conjugate-gradient local minimization, we perform 150 ps molecular dynamics (MD) at low (T=10 K) temperature, similar to the procedure developed in Refs. [63, 64], adding a harmonic force with constant k = 100 kJ mol-1 nm-2 in the yz plane to drive the fiber formation. The choice of low temperature for this equilibration part is dictated by the need to keep the well-ordered central region, responsible for the rigid beta-sheet structure of the actual protein [63, 64]. The resulting configurations are used as starting points for 500 ps MD runs at T=300 K. All calculations are performed using the Generalized-Born Surface-Accessible implicit solvent model [67] to mimic a wet environment surrounding the silk assuming a continuum model of water. Fig.S11a shows the spider-silk protein, with a β-sheet rich crystalline region and an α-helix-rich amorphous region, in good agreement with Refs. [63, 64]. Graphene does not qualitatively change this, Fig.S11b. The simulations show that graphene tends to slide out of the protein, while remaining anchored to the amorphous part. Fig.S11c indicates that CNTs tend to remain trapped within the amorphous region with two structural consequences: a slight disruption of the crystalline order of the β-sheet region, and a tendency to increase the amount of disorder in the α-helix.

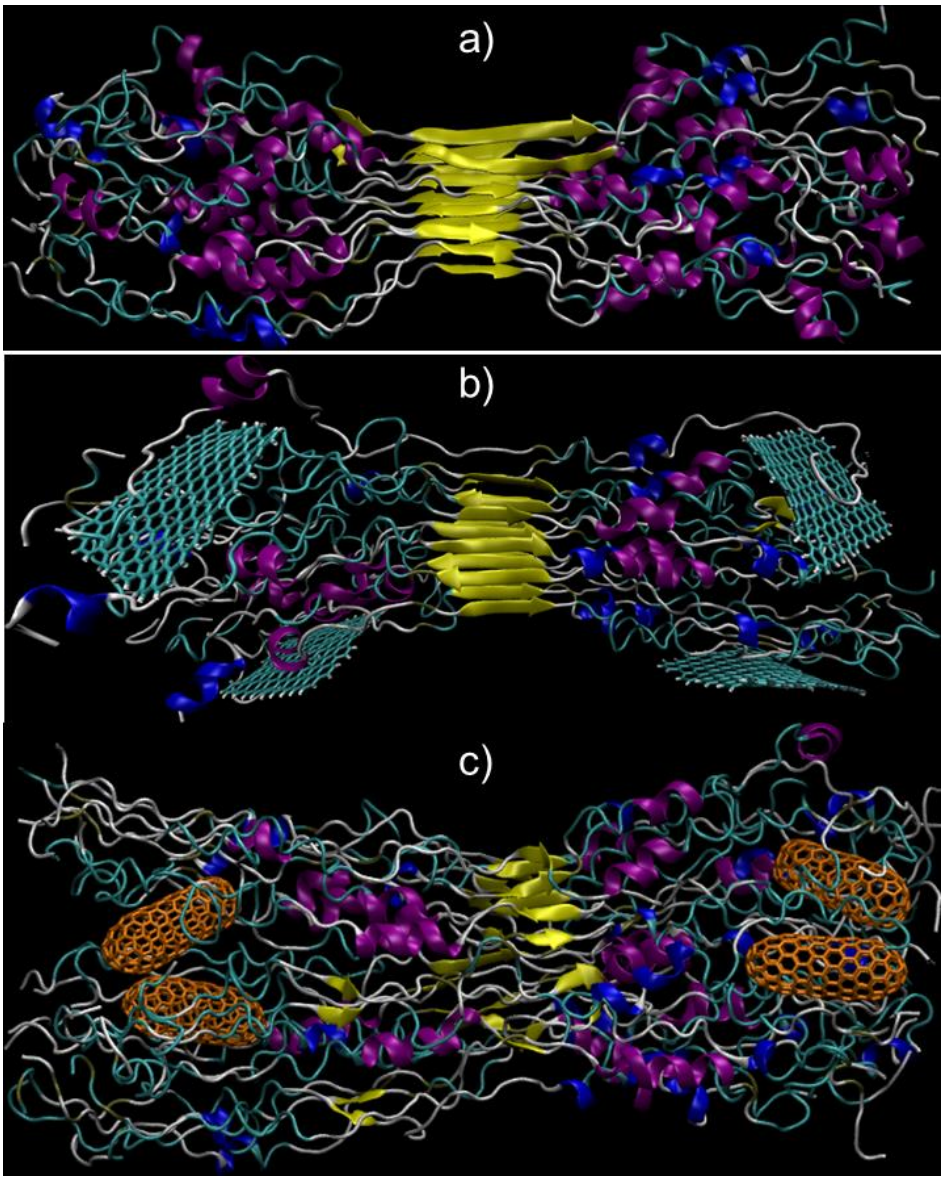

Figure S11: *Representative structures of (a) pristine MASP1 bundle, and after (b) graphene and (c) CNT incorporation. Beta sheet: yellow, alpha helix: purple, 3-10 helix: blue. Graphene is represented in green and CNTs in orange.*

References:

[1] Decreto legislativo 04 marzo 2014 , n. 26 Attuazione della direttiva 2010/63/UE sulla protezione degli animali utilizzati a fini scientifici. (G.U. Serie Generale , n. 61 del 14 marzo 2014

[2] Lide D R 1999 *CRC handbook of chemistry and physics* (Boca Raton, FL: Chapman and Hall/CRCnetBASE)

[3] Lieberman M, Marks A D, Smith C M, Marks D B and Smith C M 2007 *Marks' essential medical biochemistry* (Philadelphia: Lippincott Williams & Wilkins)

[4] Begley M, Gahan C G M and Hill C 2005 The interaction between bacteria and bile *Fems Microbiol Rev* **29** 625-51

[5] Duncan D and Rotunda A M 2011 Injectable Therapies for Localized Fat Loss: State of the Art *Clinics in Plastic Surgery* **38** 489-501

[6] Guinea G V, Elices M, Pérez-Rigueiro J and Plaza G 2003 Self-tightening of spider silk fibers induced by moisture *Polymer* **44** 5785-8

[7] Tan P H, Hasan T, Bonaccorso F, Scardaci V, Rozhin A G, Milne W I and Ferrari A C 2008 Optical properties of nanotube bundles by photoluminescence excitation and absorption spectroscopy *Physica E* **40** 2352-9

[8] Tan P H, Rozhin A G, Hasan T, Hu P, Scardaci V, Milne W I and Ferrari A C 2007 Photoluminescence spectroscopy of carbon nanotube bundles: Evidence for exciton energy transfer *Phys Rev Lett* **99**

[9] Hagen A and Hertel T 2003 Quantitative analysis of optical spectra from individual single-wall carbon nanotubes *Nano Lett* **3** 383-8

[10] Bonaccorso F, Hasan T, Tan P H, Sciascia C, Privitera G, Di Marco G, Gucciardi P G and Ferrari A C 2010 Density Gradient Ultracentrifugation of Nanotubes: Interplay of Bundling and Surfactants Encapsulation *J Phys Chem C* **114** 17267-85

[11] Curcio J A and Petty C C 1951 The Near Infrared Absorption Spectrum of Liquid Water *J. Opt. Soc. Am.* **41** 302-4

[12] Krupke R, Hennrich F, Hampe O and Kappes M M 2003 Near-infrared absorbance of single-walled carbon nanotubes dispersed in dimethylformamide *J Phys Chem B* **107** 5667-9

[13] Landi B J, Ruf H J, Worman J J and Raffaelle R P 2004 Effects of alkyl amide solvents on the dispersion of single-wall carbon nanotubes *J Phys Chem B* **108** 17089-95

[14] Kataura H, Kumazawa Y, Maniwa Y, Umezu I, Suzuki S, Ohtsuka Y and Achiba Y 1999 Optical properties of single-wall carbon nanotubes *Synthetic Met* **103** 2555-8

[15] Weisman R B and Bachilo S M 2003 Dependence of optical transition energies on structure for single-walled carbon nanotubes in aqueous suspension: An empirical Kataura plot *Nano Lett* **3** 1235-8

[16] Bachilo S M, Strano M S, Kittrell C, Hauge R H, Smalley R E and Weisman R B 2002 Structure-assigned optical spectra of single-walled carbon nanotubes *Science* **298** 2361-6

[17] Kravets V G, Grigorenko A N, Nair R R, Blake P, Anissimova S, Novoselov K S and Geim A K 2010 Spectroscopic ellipsometry of graphene and an exciton-shifted van Hove peak in absorption *Phys Rev B* **81**

[18] Torrisi F, Hasan T, Wu W P, Sun Z P, Lombardo A, Kulmala T S, Hsieh G W, Jung S J, Bonaccorso F, Paul P J, Chu D P and Ferrari A C 2012 Inkjet-Printed Graphene Electronics *Acs Nano* **6** 2992-3006

[19] Hernandez Y, Nicolosi V, Lotya M, Blighe F M, Sun Z Y, De S, McGovern I T, Holland B, Byrne M, Gun'ko Y K, Boland J J, Niraj P, Duesberg G, Krishnamurthy S, Goodhue R, Hutchison J, Scardaci V, Ferrari A C and Coleman J N 2008 High-yield production of graphene by liquid-phase exfoliation of graphite *Nat Nanotechnol* **3** 563-8

[20] Rao A M, Richter E, Bandow S, Chase B, Eklund P C, Williams K A, Fang S, Subbaswamy K R, Menon M, Thess A, Smalley R E, Dresselhaus G and Dresselhaus M S 1997 Diameter-selective Raman scattering from vibrational modes in carbon nanotubes *Science* **275** 187-91

[21] Telg H, Maultzsch J, Reich S, Hennrich F and Thomsen C 2004 Chirality distribution and transition energies of carbon nanotubes *Phys Rev Lett* **93**

[22] Meyer J C, Paillet M, Michel T, Moreac A, Neumann A, Duesberg G S, Roth S and Sauvajol J L 2005 Raman modes of index-identified freestanding single-walled carbon nanotubes *Phys Rev Lett* **95**
[23] Fantini C, Jorio A, Souza M, Strano M S, Dresselhaus M S and Pimenta M A 2004 Optical transition energies for carbon nanotubes from resonant Raman spectroscopy: Environment and temperature effects *Phys Rev Lett* **93**
[24] Paillet M, Michel T, Meyer J C, Popov V N, Henrard L, Roth S and Sauvajol J L 2006 Raman active phonons of identified semiconducting single-walled carbon nanotubes *Phys Rev Lett* **96**
[25] Jorio A, Saito R, Hafner J H, Lieber C M, Hunter M, McClure T, Dresselhaus G and Dresselhaus M S 2001 Structural (n, m) determination of isolated single-wall carbon nanotubes by resonant Raman scattering *Phys Rev Lett* **86** 1118-21
[26] O'Connell M J, Bachilo S M, Huffman C B, Moore V C, Strano M S, Haroz E H, Rialon K L, Boul P J, Noon W H, Kittrell C, Ma J P, Hauge R H, Weisman R B and Smalley R E 2002 Band gap fluorescence from individual single-walled carbon nanotubes *Science* **297** 593-6
[27] Shi Z, Lian Y, Zhou X, Gu Z, Zhang Y, Iijima S, Zhou L, Yue K T and Zhang S 1999 Mass-production of single-wall carbon nanotubes by arc discharge method1 *Carbon* **37** 1449-53
[28] Araujo P T, Jorio A, Dresselhaus M S, Sato K and Saito R 2009 Diameter Dependence of the Dielectric Constant for the Excitonic Transition Energy of Single-Wall Carbon Nanotubes *Phys Rev Lett* **103**
[29] Ferrari A C 2007 Raman spectroscopy of graphene and graphite: Disorder, electron-phonon coupling, doping and nonadiabatic effects *Solid State Commun* **143** 47-57
[30] Ferrari A C, Meyer J C, Scardaci V, Casiraghi C, Lazzeri M, Mauri F, Piscanec S, Jiang D, Novoselov K S, Roth S and Geim A K 2006 Raman spectrum of graphene and graphene layers *Phys Rev Lett* **97**
[31] Ferrari A C and Robertson J 2000 Interpretation of Raman spectra of disordered and amorphous carbon *Phys Rev B* **61** 14095-107
[32] Tuinstra F and Koenig J L 1970 Raman Spectrum of Graphite *The Journal of Chemical Physics* **53** 1126-30
[33] Ferrari A C and Basko D M 2013 Raman spectroscopy as a versatile tool for studying the properties of graphene *Nat Nanotechnol* **8** 235-46
[34] Mohiuddin T M G, Lombardo A, Nair R R, Bonetti A, Savini G, Jalil R, Bonini N, Basko D M, Galiotis C, Marzari N, Novoselov K S, Geim A K and Ferrari A C 2009 Uniaxial strain in graphene by Raman spectroscopy: G peak splitting, Gruneisen parameters, and sample orientation *Phys Rev B* **79**
[35] Piscanec S, Lazzeri M, Robertson J, Ferrari A C and Mauri F 2007 Optical phonons in carbon nanotubes: Kohn anomalies, Peierls distortions, and dynamic effects *Phys Rev B* **75**
[36] Jorio A, Souza A G, Dresselhaus G, Dresselhaus M S, Swan A K, Unlu M S, Goldberg B B, Pimenta M A, Hafner J H, Lieber C M and Saito R 2002 G-band resonant Raman study of 62 isolated single-wall carbon nanotubes *Phys Rev B* **65**
[37] Lazzeri M, Piscanec S, Mauri F, Ferrari A C and Robertson J 2006 Phonon linewidths and electron-phonon coupling in graphite and nanotubes *Phys Rev B* **73**
[38] Tsang J C, Freitag M, Perebeinos V, Liu J and Avouris P 2007 Doping and phonon renormalization in carbon nanotubes *Nat Nanotechnol* **2** 725-30
[39] Das A, Pisana S, Chakraborty B, Piscanec S, Saha S K, Waghmare U V, Novoselov K S, Krishnamurthy H R, Geim A K, Ferrari A C and Sood A K 2008 Monitoring dopants by Raman scattering in an electrochemically top-gated graphene transistor *Nat Nanotechnol* **3** 210-5
[40] Das A, Sood A K, Govindaraj A, Saitta A M, Lazzeri M, Mauri F and Rao C N R 2007 Doping in carbon nanotubes probed by Raman and transport measurements *Phys Rev Lett* **99**
[41] Shiozawa H, Pichler T, Kramberger C, Rummeli M, Batchelor D, Liu Z, Suenaga K, Kataura H and Silva S R P 2009 Screening the Missing Electron: Nanochemistry in Action *Phys Rev Lett* **102**
[42] Hasan T, Torrisi F, Sun Z, Popa D, Nicolosi V, Privitera G, Bonaccorso F and Ferrari A C 2010 Solution-phase exfoliation of graphite for ultrafast photonics *Phys Status Solidi B* **247** 2953-7
[43] Casiraghi C, Hartschuh A, Lidorikis E, Qian H, Harutyunyan H, Gokus T, Novoselov K S and Ferrari A C 2007 Rayleigh imaging of graphene and graphene layers *Nano Lett* **7** 2711-7
[44] Wang Q, Wang C Y, Zhang M C, Jian M Q and Zhang Y Y 2016 Feeding Single-Walled Carbon Nanotubes or Graphene to Silkworms for Reinforced Silk Fibers *Nano Lett* **16** 6695-700

[45] Brown C P, MacLeod J, Amenitsch H, Cacho-Nerin F, Gill H S, Price A J, Traversa E, Licoccia S and Rosei F 2011 The critical role of water in spider silk and its consequence for protein mechanics *Nanoscale* **3** 3805-11
[46] Agnarsson I, Dhinojwala A, Sahni V and Blackledge T A 2009 Spider silk as a novel high performance biomimetic muscle driven by humidity *J Exp Biol* **212** 1989-93
[47] Vollrath F, Madsen B and Shao Z Z 2001 The effect of spinning conditions on the mechanics of a spider's dragline silk *P Roy Soc B-Biol Sci* **268** 2339-46
[48] Liu Y, Shao Z Z and Vollrath F 2005 Relationships between supercontraction and mechanical properties of spider silk *Nat Mater* **4** 901-5
[49] Collins P G and Avouris P 2000 Nanotubes for electronics *Sci Am* **283** 62-+
[50] Atkins E 2003 Silk's secrets *Nature* **424** 1010-
[51] Stankovich S, Dikin D A, Dommett G H B, Kohlhaas K M, Zimney E J, Stach E A, Piner R D, Nguyen S T and Ruoff R S 2006 Graphene-based composite materials *Nature* **442** 282-6
[52] Kosynkin D V, Higginbotham A L, Sinitskii A, Lomeda J R, Dimiev A, Price B K and Tour J M 2009 Longitudinal unzipping of carbon nanotubes to form graphene nanoribbons *Nature* **458** 872-U5
[53] Young R J, Kinloch I A, Gong L and Novoselov K S 2012 The mechanics of graphene nanocomposites: A review *Compos Sci Technol* **72** 1459-76
[54] Vehoff T, Glisovic A, Schollmeyer H, Zippelius A and Salditt T 2007 Mechanical properties of spider dragline silk: Humidity, hysteresis, and relaxation *Biophys J* **93** 4425-32
[55] Swanson B O, Blackledge T A, Summers A P and Hayashi C Y 2006 Spider dragline silk: correlated and mosaic evolution in high-performance biological materials *Evolution* **60** 2539-51
[56] Blackledge T A and Hayashi C Y 2006 Silken toolkits: biomechanics of silk fibers spun by the orb web spider Argiope argentata (Fabricius 1775) *Journal of Experimental Biology* **209** 2452-61
[57] Agnarsson I, Kuntner M and Blackledge T A 2010 Bioprospecting Finds the Toughest Biological Material: Extraordinary Silk from a Giant Riverine Orb Spider *Plos One* **5** e11234
[58] Weibull W 1951 A statistical distribution function of wide applicability *J. Appl. Mech* **18** 293–7
[59] Pugno N M, Bosia F and Carpinteri A 2008 Multiscale stochastic simulations for tensile testing of nanotube-based macroscopic cables *Small* **4** 1044-52
[60] Ruoff R S, Qian D and Liu W K 2003 Mechanical properties of carbon nanotubes: theoretical predictions and experimental measurements *Cr Phys* **4** 993-1008
[61] Lee C, Wei X D, Kysar J W and Hone J 2008 Measurement of the elastic properties and intrinsic strength of monolayer graphene *Science* **321** 385-8
[62] Lepore E, Bonaccorso, F., Bruna, M., Bosia, F., Taioli, S. Garberoglio, G., Ferrari, A. C., Pugno, N.M. 2015 Silk reinforced with graphene or carbon nanotubes spun by spiders *arXiv:1504.06751 [cond-mat.mtrl-sci]*
[63] Keten S and Buehler M J 2010 Atomistic model of the spider silk nanostructure *Appl Phys Lett* **96**
[64] Keten S and Buehler M J 2010 Nanostructure and molecular mechanics of spider dragline silk protein assemblies *J R Soc Interface* **7** 1709-21
[65] Hess B, Kutzner C, van der Spoel D and Lindahl E 2008 GROMACS 4: Algorithms for highly efficient, load-balanced, and scalable molecular simulation *J Chem Theory Comput* **4** 435-47
[66] O'Boyle N M, Banck M, James C A, Morley C, Vandermeersch T and Hutchison G R 2011 Open Babel: An open chemical toolbox *J Cheminformatics* **3**
[67] Larsson P and Lindahl E 2010 A High-Performance Parallel-Generalized Born Implementation Enabled by Tabulated Interaction Rescaling *J Comput Chem* **31** 2593-600